Molecular properties of RmlT, a wall teichoic acid rhamnosyltransferase that modulates *Listeria monocytogenes* virulence and antibiotic resistance

Ricardo Monteiro[1,2,#,*],Tatiana B. Cereija[1,2,#], Rita Pombinho[1,2], Sandra Sousa[1,2], João H. Morais-Cabral[1,2,$] and Didier Cabanes[1,2,$,*]

[1] i3S – Instituto de Investigação e Inovação em Saúde, Universidade do Porto, Porto, Portugal

[2] IBMC – Instituto de Biologia Molecular e Celular, Universidade do Porto, Porto, Portugal

* Corresponding authors: didier@i3s.up.pt; ricardo.monteiro@i3s.up.pt

[#] These authors contributed equally
[$] These authors share last authorship

Abstract

Wall teichoic acids (WTA) from the major Gram-positive foodborne pathogen *Listeria monocytogenes* are peptidoglycan-associated glycopolymers decorated by monosaccharides that, while not essential for bacterial growth, are required for bacterial virulence and resistance. Here we report the first structure and function of a bacterial WTA rhamnosyltransferase, RmlT, strictly required for *L. monocytogenes* WTA rhamnosylation. We demonstrated that RmlT transfers rhamnose from TDP-rhamnose to naked WTA, and that specificity towards TDP-rhamnose is kinetically determined. We solved the RmlT structure, identified key residues for its activity and showed that RmlT behaves as a dimer whose interface is important for its stability and function. We propose that RmlT undergoes a transition between an open and closed conformation, allowing RmlT to first bind WTA and then trapping it inside the tunnel formed by the catalytic, oligomerization and helical subdomains. Finally, we proved that mutation of a single residue in the RmlT active site leads to enzyme inactivation and decreased infection *in vivo*, confirming WTA glycosyltransferases as promising targets for next-generation strategies against Gram-positive pathogens.

Introduction

Infections caused by Gram-positive bacteria remain a major public health burden and a main challenge in medicine. We witness the emergence of not only new pathogens but also new bacterial strains with altered virulence properties and/or increased antimicrobial resistance [1]. Among them, *Listeria monocytogenes* is the Gram-positive foodborne pathogen that accounts for the highest proportion of hospitalisation cases and number of deaths due to food poisoning in Europe, with emergence of antibiotic resistances [1, 2]. The cell wall of *L. monocytogenes* and other Gram-positive bacteria is a thick mesh-like complex that maintains cellular integrity. It is composed of three major constituents, namely the peptidoglycan backbone, anionic teichoic acid polymers and wall-associated proteins. Teichoic acids are the vast majority of cell wall carbohydrates, either associated to the peptidoglycan (wall teichoic acids or WTA) or bound directly to the cytoplasmic membrane (lipoteichoic acids or LTA) [3]. While the basic structure of LTA remains relatively conserved among different Gram-positive species and serovars [4-8], WTA display significant structural and constitutional diversity, as well as a variety of glycosylation patterns, resulting in different fitness outcomes such as biofilm formation, virulence capacity and resistance to bacteriophages and antimicrobials [4, 9-21]. WTA are complex glycopolymers made of 20 to 30 repeating units of ribitol-phosphate (RboP). In *Staphylococcus aureus*, the polymeric RboP backbone of WTA is modified through the addition of *N*-acetylglucosamine (GlcNAc) moieties by different glycosyltransferases, including TarM, TarS, and TarP, which have different specificities. While TarM is responsible for α-GlcNAc glycosylation at position *C*-4 of the ribitol unit, TarS and TarP are required for the β-GlcNAc glycosylation at positions *C*-4 and *C*-3, respectively [22-24]. Interestingly, all these individual GlcNAc additions to the poly-RboP chain have dramatic impact on pathogen-host interactions [25]. The molecular properties of the *S. aureus* WTA glycosyltransferases have been characterized [24-27].

L. monocytogenes WTA are grouped in two subtypes: i) Type I WTA, made of repeating units of 1,5-phosphodiester-linked ribitol glycosylated with GlcNAc at position *C*-2 and rhamnose at position *C*-4 in serovar 1/2, with GlcNAc at position *C*-4 in serovar 3, or unglycosylated in serovar 7; and ii) Type II WTA, that contain GlcNAc at positions *C*-2 in serovars 4a, 4c, 5, 6b or at *C*-4 in serovars 4b, 4d, 4e, 4h and 6a in addition to other modifications with glucose, galactose or GlcNAc moieties, or with phosphate or acetyl groups [4, 20].

We previously performed the first genome-wide transcriptome of a bacterial pathogen infecting a host deep organ using *L. monocytogenes* EGDe (serovar 1/2a) strain as model pathogen. This study revealed that genes responsible for the biosynthesis of TDP-rhamnose (*rmlABCD*) and

the transfer of the rhamnose moiety to WTA (*rmlT*) are highly expressed during *in vivo* infection [28]. Importantly, we showed that WTA rhamnosylation is required for the proper association of major virulence factors to the bacterial surface [14], and for resistance to antimicrobial peptides [13] and antibiotics [16]. In addition, we showed that WTA decoration with rhamnose is strictly dependent on the rhamnosyltransferase RmlT [13]. Altogether, our previous data revealed that, although dispensable for bacterial growth, RmlT has a significant impact on bacterial virulence and antimicrobial resistance.

Here, we explored the molecular properties of RmlT. Using a combination of structural and biochemical approaches, we solved the structure of RmlT, uncovered its oligomeric organization, identified the molecular determinants of donor-substrate binding and specificity, and demonstrated that, by blocking RmlT activity, we can significantly reduce bacterial virulence, pointing this rhamnosyltransferase as promising target for new anti-virulence strategies.

Results

Enzymatic activity of the *L. monocytogenes* rhamnosyltransferase RmlT

We previously showed that RmlT is required for WTA rhamnosylation in *L. monocytogenes* [13]. To confirm that RmlT is indeed capable of transferring rhamnose to WTA, we set-up an *in vitro* enzymatic assay using TDP-rhamnose as donor substrate and naked WTA as acceptor substrate. Naked WTA were isolated from *L. monocytogenes* EGDe Δ*rmlT*Δ*lmo1079* strain that lacks the ability to produce both RmlT and Lmo1079, respectively reported to be involved in the addition of rhamnose and GlcNAc moieties to WTA [13, 29]. RmlT enzymatic activity was evaluated by analysing in parallel the reaction products: decorated WTA and TDP.

Decoration of WTA was analyzed by electrophoretic mobility shift assay. After incubation with TDP-rhamnose and purified RmlT, WTA showed a change in migration, with bands running higher in a native gel and displaying a more diffuse appearance compatible with glycosylated material (Figure 1A). The generation of TDP by RmlT when transferring rhamnose to WTA was quantified indirectly using a coupled functional assay that measures the amount of free phosphate generated by a phosphatase from the TDP produced by RmlT activity (Figure 1B). The amount of phosphate detected in the reaction mixture containing TDP-rhamnose, WTA and RmlT was significantly higher than in the reaction mixture lacking RmlT. The generation of TDP only happens when naked WTA is present, showing that RmlT is not capable of hydrolyzing TDP-rhamnose to TDP and rhamnose in the absence of the acceptor substrate WTA. Together, these experiments strongly indicate that RmlT transfers rhamnose from TDP-rhamnose to naked WTA, producing TDP and rhamnosylated WTA.

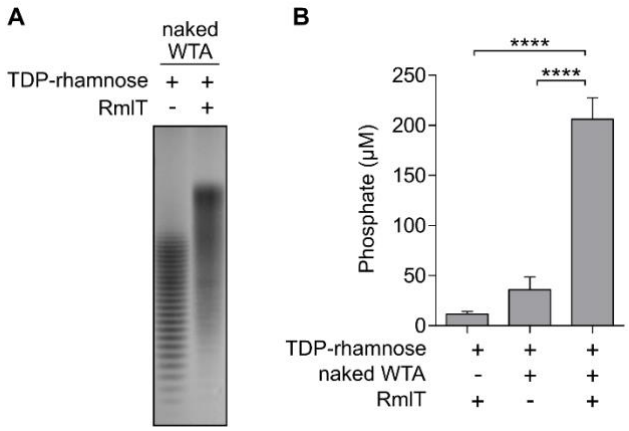

Figure 1: RmlT transfers rhamnose from TDP-rhamnose to naked WTA. A) Electrophoretic mobility shift assay of the reaction mixture containing naked WTA and TDP-rhamnose, in the absence (-) and presence (+) of RmlT. The individual bands observed in each lane correspond to different WTA chains. B) Coupled function assay quantifies the amount of

phosphate released after hydrolysis of TDP molecules generated by RmlT. In both assays reactions ran for 60 minutes with 5 mM WTA, 1 mM TDP-rhamnose and 10 µM RmlT. Values are the mean ± SD (n = 3). The *p*-values were calculated using a one-way ANOVA; **** $p < 0.0001$.

Structure of RmlT

To gain insights into the molecular properties of *L. monocytogenes* RmlT, we determined its crystal structure in the apo state at ~2.5 Å. Globally, RmlT presents the characteristic architecture of other glycosyltransferases like the *S. aureus* TarS and TarP [24, 27], with a catalytic region at the N-terminus and an oligomerization region at the C-terminus (Figure 2A and Supplementary Figure 1A). Running from the N to the C terminus, RmlT shows a catalytic subdomain strongly connected to a helical subdomain, a large oligomerization subdomain and a turret subdomain (Figure 2A). Comparison between RmlT, TarS and TarP (all classified as members of the GT2 family of glycosyl transferases in CAZy, http://www.cazy.org/), showed strong similarities at the level of the catalytic subdomains of the three enzymes (Figure 2B), while the helical, oligomerization and turret subdomains of RmlT are very similar to the equivalent regions in TarS (Supplementary Figure 1A). Interestingly, it has been shown that the oligomerization and turret domains of TarS stand apart from the catalytic domain, adopting different dispositions that are suggestive of flexibility [27]. In contrast, the oligomerization domain of RmlT lies over the catalytic domain, establishing an extensive interaction surface (~480 $Å^2$) (Figure 2A and Supplementary Figure 1A). In addition, the connection between the helical and oligomerization subdomains is established in TarS by a 4 amino acid linker (residues 349-352) while in RmlT three linkers (residues 340-342, 368-388 and 406-410) run between the subdomains (Supplementary Figure 1B).

Contrasting with Tar proteins that form trimers (Supplementary Figure 1C) [27], RmlT eluted in a size-exclusion chromatography column with an apparent molecular weight compatible with a dimer (Supplementary Figure 2) and assembles as a dimer in the crystal with the oligomerization subdomains interacting in an antiparallel arrangement and positioning the catalytic subdomains at opposite corners of a rectangular shape (Figure 2C). To assess the functional impact of the dimeric architecture of RmlT, we generated structure-guided mutants ($RmlT_{Y368A+E372A}$ and $RmlT_{Y347A+Y368A+E372A}$) that aimed at disrupting the dimerization interface (Figure 2C). Attempts to express and purify mutant proteins resulted in aggregated protein, supporting the role of these residues in dimer formation. The impact of mutations of the RmlT dimerization interface was also tested *in vivo* using a bacteriophage rhamnose binding protein (gp17), that specifically binds to rhamnose at the *L. monocytogenes* bacterial surface, fused to GFP (gp17-GFP) [24]. Exponentially

growing bacteria were incubated with gp17-GFP and fluorescence associated with the bacterial cell wall staining was quantified in a plate format and visualized by fluorescence microscopy (Figure 2D-E). Deletion of *rmlT* in the *L. monocytogenes* EGDe strain resulted in a very significant decrease in the fluorescence intensity to residual levels, which was restored by complementation with *rmlT*, confirming the role of RmlT in the rhamnosylation of the *L. monocytogenes* cell surface. Complemention with the *rmlT* dimerization interface mutants significantly reduced, but did not abolish, fluorescence intensity (Figure 2D). Fluorescence microscopy showed that the surface of bacteria expressing the dimerization mutants is still rhamnosylated but show an altered pattern, with staining restricted to the poles (Figure 2E). Altogether, these data strongly suggest that RmlT is a dimer in solution and that changes in dimer formation impact its stability and, consequently, its physiological function.

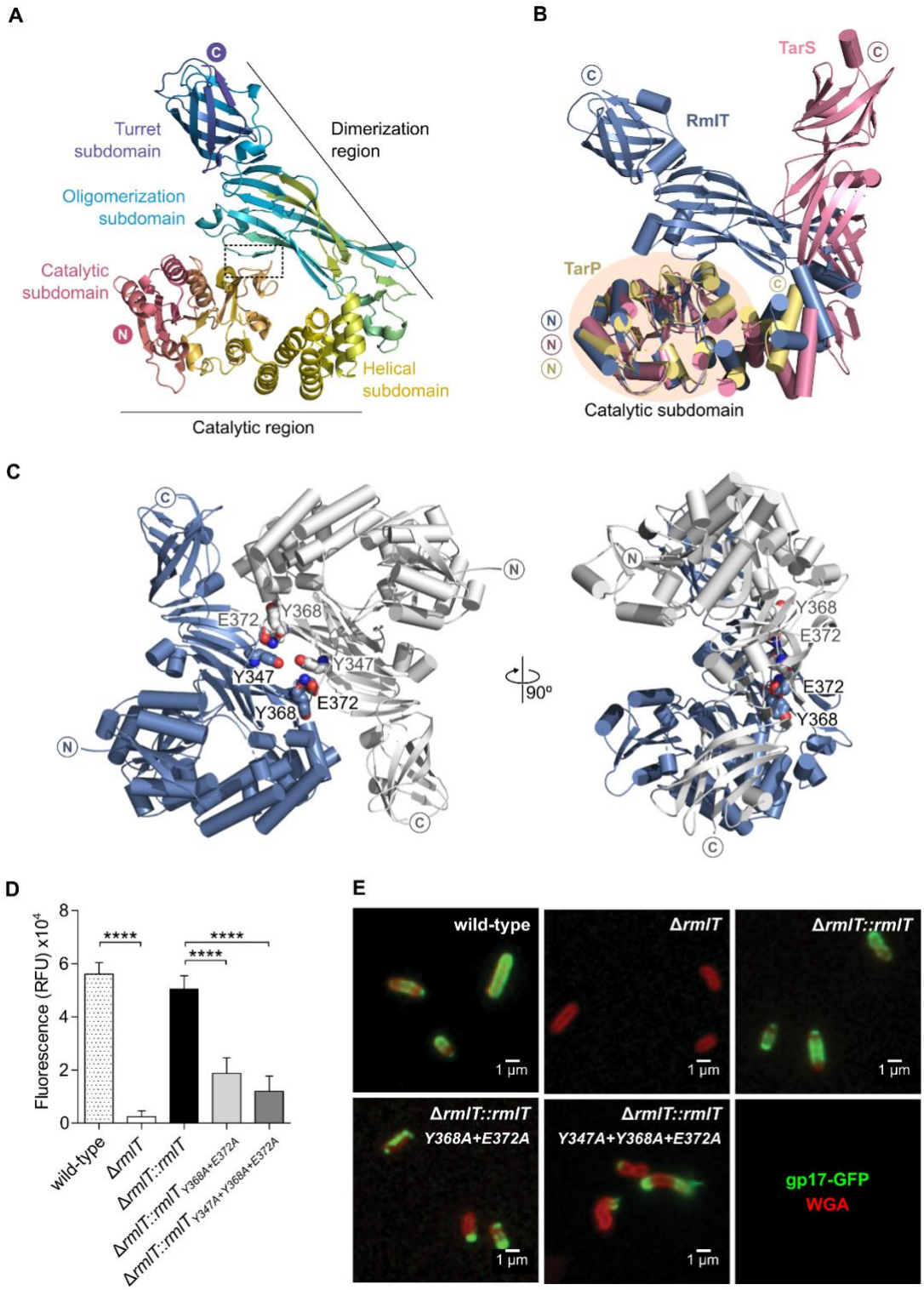

Figure 2: Structure of *L. monocytogenes* RmlT. A) Cartoon representation of a subunit of RmlT colored from pink at N terminus to purple at C terminus with subdomains and N and C termini indicated. The catalytic region includes the catalytic and helical subdomains. The dimerization region includes the oligomerization and turret subdomains. The interaction between catalytic and oligomerization subdomains is indicated by the dashed rectangle (PDB code: 8BZ4). B) Superposition of RmlT (blue, PDB code: 8BZ4) and *S. aureus* TarS (pink, PDB code: 5TZ8) and TarP (yellow, PDB code: 6H1J) through their catalytic subdomains (wheat ellipse). C) Two views of RmlT dimer showing subunits colored blue and white and with dimerization interface residues Y347, Y368 and E372 as spheres (PDB code: 8BZ4). D)

Quantification of the fluorescence associated to gp17-GFP bound to rhamnose at the surface of the *L. monocytogenes* strains EGDe Δ*rmlT::rmlT,* EGDe Δ*rmlT::rmlT*$_{Y368A+E372A}$ and EGDe Δ*rmlT::rmlT*$_{Y347A+Y368A+E372A}$. Wild-type *L. monocytogenes* EGDe and EGDe Δ*rmlT* were used as positive and negative controls, respectively. Values are mean ± SD (n = 3); one-way ANOVA, **** = $p < 0.0001$. E) Fluorescence microscopy images of *L. monocytogenes* cells stained with wheat germ agglutinin (WGA, red) and gp17-GFP (green) which binds to rhamnose at the bacterial surface.

RmlT active site

The structure of RmlT with bound TDP-rhamnose was solved at 2.2 Å with 6 subunit copies in the asymmetric unit (Figure 3A). The electron-density for the ligand is clear and it was straightforward to build the nucleoside moiety in the catalytic subdomain. However, there is a lack of detail in the electron-density for the sugar (Supplementary Figures 3A-B). In addition, superposition of the 6 copies of RmlT/TDP-rhamnose revealed that while the nucleotide base and deoxyribose groups are spatially invariant between copies, sugar moieties in the TDP-rhamnose complex do not adopt exactly the same conformation or the same position across the different protein subunits, indicating that the sugar is not as firmly anchored to the protein as the nucleoside (Supplementary Figure 4A).

Comparison of catalytic subdomains of RmlT/TDP-rhamnose, TarP/UDP-GlcNAc (PDB code: 6H2N) and TarS/UDP-GlcNAc (PDB code: 5TZE) showed that many of the molecular interactions established by the nucleoside moiety of the donor substrate involve conserved residues (Supplementary Figures 5-6). In particular, in RmlT (Figure 3A) the nucleotide base is hydrogen bonded to D59 and N86, while the deoxyribose hydroxyl interacts with the main-chain carbonyl of the conserved P26 and amino group of H111. In addition, D112 and D113 together with the phosphate groups of the nucleotide are involved in the coordination of a single Mg^{2+}. D112 coordinates the cation directly while D113 interacts *via* two water molecules, just like in the other two enzymes (Supplementary Figure 5). The conserved residue D110 lines the bottom of the binding pocket by interacting with the also conserved R94. Of the interactions between the rhamnose and the protein, those involving E197 and D198 standout as these residues are conserved in TarP and TarS and are considered to be crucial for catalysis (Figure 3A and supplementary Figure 5) [24, 27]. In addition, two non-conserved tryptophans (W89 and W223) also interact with the sugar (Supplementary Figure 5). The position of W89 varies between RmlT copies (Figure 3B) but that of W223 is invariant and is within hydrogen bond distance of the sugar oxygen (*O*1), raising the hypothesis that it contributes to the polarization of the anomeric carbon promoting the catalytic reaction.

In addition to the structures of apo-RmlT described above, with 2 copies in the asymmetric unit, and of RmlT/TDP-rhamnose complex (6 copies), we also determined another RmlT apo-structure with 4 copies per asymmetric unit at a slightly higher resolution (2.3 Å). Globally, there are only minor changes between bound and unbound structures. However, while in the nucleotide-bound subunits there is little structural variability in the catalytic subdomain (Figures 3A and 3C), we observed a large degree of freedom in the apo-structures (Figures 3B and D), reflecting the absence of stabilizing interactions with the ligand. In particular, the major structural variability in the catalytic subdomain occurs in two loops, loops A (residues 86-90) and B (residues 190-195). In one of the apo-protein copies the loop 86-90 flips away from the binding site and W89 (already described above as interacting with the rhamnose in the RmlT complex) points towards the bulk solvent.

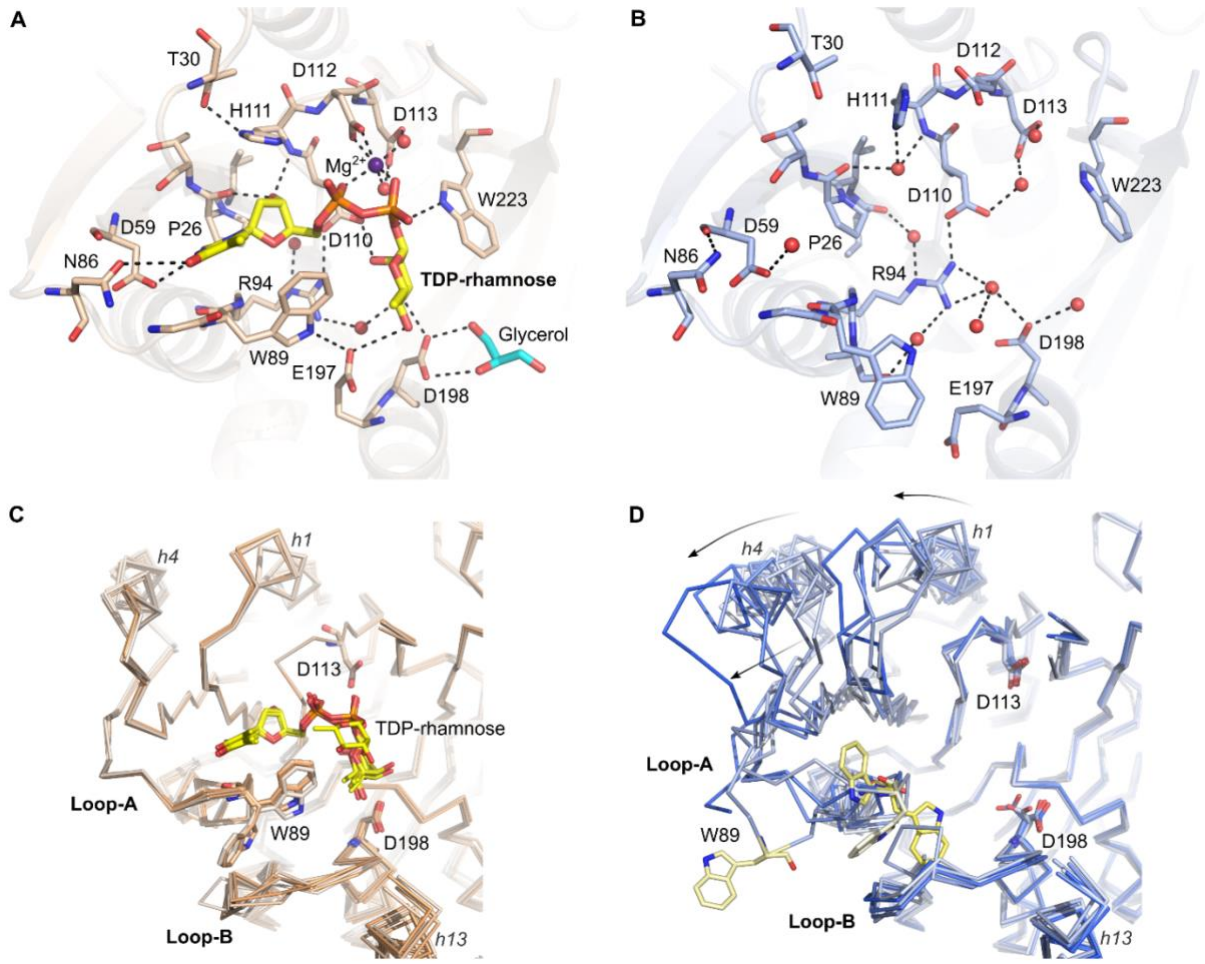

Figure 3: Active site of RmlT. A) Cartoon representation of the active-site region of RmlT with TDP-rhamnose and the interacting residues represented as sticks (PDB code: 8BZ7). Glycerol molecule used as cryo-protectant was found interacting with D198, likely mimicking a ribitol molecule. B) Cartoon representation of the active-site region of the apo RmlT with donor substrate interaction residues represented as sticks (PDB code: 8BZ4). Water molecules and Mg^{2+} are shown as red and purple spheres, respectively. Hydrogen bonds are shown as dashed black lines. C) Superposed active-sites of all RmlT/TDP-rhamnose subunits present in the asymmetric unit colored in different shades of wheat (PDB code:

8BZ7). TDP-rhmanose and some substrate-interacting residues are shown as sticks. D) Superposed active-sites of apo RmlT subunits present in the asymmetric unit in two different crystal forms, colored in different shades of blue (PDB codes: 8BZ4 and 8BZ5). Some substrate-interacting residues are represented as sticks with W89 in yellow. Loops A and B and helices *h*1, *h*4 and *h*13 are indicated. Flexibility of the *h*1 and *h*4 is represented by the arrows.

To evaluate the functional impact of some of the residues in the catalytic subdomain, we generated single-point alanine mutants at the active-site residues E197, D198, W89 and W223 (Figure 3A). Recombinant RmlT mutants were incubated with naked WTA and TDP-rhamnose, and the reaction was quantified by the free-phosphate coupled function assay (Figure 4A). As expected, mutation of E197 or D198 resulted in a complete loss of *in vitro* activity, fitting with their proposed role in catalysis. W223A had wild-type levels of activity, showing that this residue is not important for the catalytic reaction. In contrast, W89A resulted in a loss of function, supporting the idea that W89 has a role in the proper positioning of the sugar.

To explore further the role of D198, which in TarS and TarP has been proposed to promote the nucleophilic attack of the ribitol [24, 27], we determined the structure of the mutant $RmlT_{D198A}$ in complex with TDP-rhamnose. The 6 copies of the protein are occupied by nucleotide and are for the most part identical to the structures of wild-type RmlT (Supplementaty Figure 4B). The major difference relates to the position of the sugar moiety. While in 5 out of 6 copies present in the asymmetric unit of wild-type RmlT the sugar is positioned deep inside the active site (Supplementary Figures 3A and 4A), in the $RmlT_{D198A}$ mutant structure the sugar has moved away in all 6 copies in the asymmetric unit (Figure 4B and Supplementary Figures 3C and 4B). This suggests that D198 has a role in positioning the sugar, in agreement with the observation of contacts with the rhamnose in the RmlT/TDP-rhamnose structure.

We also evaluated the impact of mutants for residues in the catalytic subdomain *in vivo*. The *L. monocytogenes* EGDe Δ*rmlT* strain was complemented with wild-type RmlT or RmlT mutants ($RmlT_{W89A,}$ $RmlT_{E197A}$, $RmlT_{D198A}$, and $RmlT_{W223A}$), and the effect of each mutation was analyzed using the gp17-GFP rhamnose binding protein. Mutations of W89, E197 and D198 completely abolished rhamnose from the bacterial surface (Figures 4C-D), confirming their importance for RmlT activity. Surprisingly, W223A also induced the absence of surface rhamnosylation, which suggests that the mutation affected a property of RmlT that is specific to its physiological function *in vivo* other than catalytic activity.

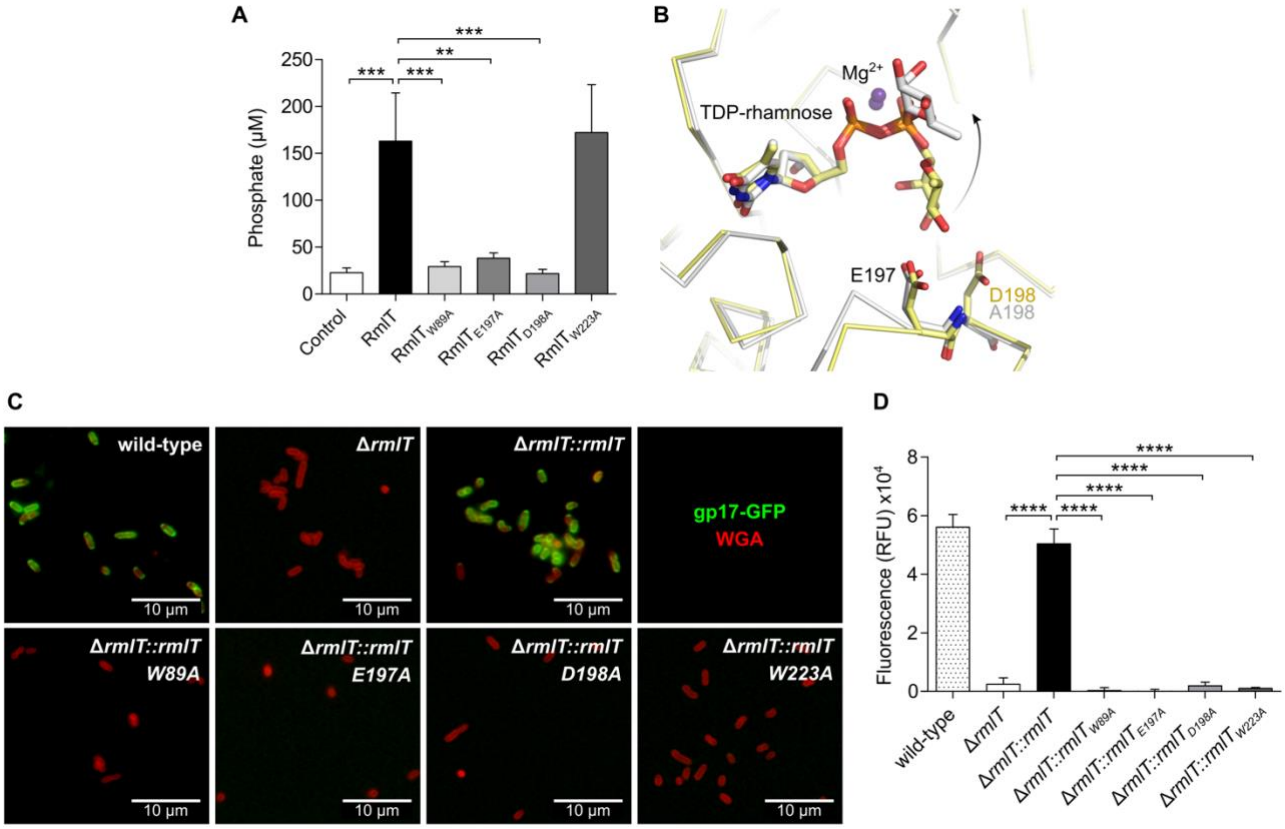

Figure 4: Impact of active-site residues in RmlT activity. A) Quantification of the amount of phosphate released from the product generated by RmlT, $RmlT_{W89A}$, $RmlT_{E197A}$, $RmlT_{D198A}$ and $RmlT_{W223A}$. Quantification was done at 30 minutes from reaction mixtures containing 1 mM WTA, 200 µM TDP-rhamnose and 2 µM RmlT. Control was the reaction without RmlT. Values are the mean ± SD (n = 3). The *p*-values were calculated using a one-way ANOVA; ** $p < 0.01$, *** $p < 0.001$. B) Superposition of the active-site region of RmlT (light yellow, PDB code: 8BZ7) and $RmlT_{D198A}$ (grey, PDB code: 8BZ8) variants in complex with TDP-rhamnose. Rhamnose moiety is stabilized by E197 and D198, and the substitution of D198 by an alanine weakens this interaction leading to a change in the position of rhamnose moiety (indicated by the arrow). C) Impact of mutations in the active site of RmlT on *L. monocytogenes* surface rhamnosylation. Fluorescence microscopy analysis of *L. monocytogenes* strains EGDe wild-type, EGDe Δ*rmlT* and EGDe Δ*rmlT* complemented with *rmlT*, $rmlT_{W89A}$, $rmlT_{E197A}$, $rmlT_{D198A}$ or $rmlT_{W223A}$. Bacterial cells and the rhamnose at the bacterial surface were stained with wheat germ agglutinin (WGA, red) and gp17-GFP rhamnose binding protein (green), respectively. *L. monocytogenes* strains EGDe and EGDe Δ*rmlT* were used as positive and negative control, respectively. D) Quantification of the fluorescence associated to gp17-GFP bound to rhamnose at the surface of the strains in C. Values are mean ± SD (n = 3). The *p*-values were calculated using one-way ANOVA; **** $p < 0.0001$.

RmlT specifity for TDP-rhamnose is kinetically determined

The lack of strong contacts between the rhamnose and RmlT residues raised the possibility that the enzyme is not selective relative to the donor substrate. To explore this hypothesis, we measured RmlT activity using the free-phosphate coupled function assay in the presence of naked WTA and the nucleotides TDP-rhamnose, TDP-glucose, UDP-glucose and UDP-GlcNAc as well as L-rhamnose.

The amount of phosphate detected was higher with TDP-rhamnose relative to all other donor substrates tested, demonstrating a catalytic preference of RmlT for this nucleotide (Figure 5A).

To evaluate in more detail the molecular basis of RmlT specificity, we used isothermal titration calorimetry (ITC) to determine its affinity for different donor substrates in the absence of WTA (Figure 5B). TDP-rhamnose bound to RmlT with a K_D of ~5 µM, with 1 molecule bound per RmlT subunit. Surprisingly, TDP-glucose bound RmlT as well as TDP-rhamnose (K_D = ~4 µM). Moreover, TDP also bound RmlT with similar affinity (K_D = ~2 µM). We could not detect binding of UDP-glucose in the experimental conditions used. These results indicate that the nucleotide moiety (TDP) determines the strength of the interaction between the donor substrate and RmlT.

Using a high concentration (5 mM) of UDP-glucose, we determined the structure of its complex with RmlT at 2.4 Å (Figure 5C). The structure reveals few changes relative to RmlT/TDP-rhamnose and does not provide obvious hints for the preference towards TDP. The two nucleotides, TDP and UDP, differ in two chemical groups, a methyl group in the thymidine and a hydroxyl group in the ribose of UDP (Figure 5D). The methyl group in the base is within Van der Waals distance of Y28 but generally points away from the protein, while the extra hydroxyl in UDP is within hydrogen bonding distance of P26 main-chain carbonyl and appears to be accommodated with very slight changes in the protein. We also searched for clues that could explain a preference for rhamnose over glucose. Interestingly, the position and conformation of the sugar in UDP-glucose is significantly better defined than that of the rhamnose in the TDP-rhamnose structures (Supplementary Figures 3E-F and 4C). This could reflect that the glucose is better stabilized in the sugar binding pocket resulting in reduced ability to acquire the proper position for catalysis when the acceptor WTA is present. Moreover, while the glucose moiety in UDP-glucose establishes hydrogen bonds with E197, rhamnose in TDP-rhamnose is hydrogen bound to D198 (as discussed above).

Altogether, our results show that selection of the donor nucleotide does not result from interactions between the sugar and RmlT, but is determined in the ternary complex either by the affinity of the donor in the presence of WTA or by the efficiency of catalysis so that the reaction proceeds faster in the presence of the correct sugar.

To determine which one of these hypotheses explains our results, we performed a competition experiment. We mixed RmlT with naked WTA in the presence of the same concentrations of TDP-rhamnose, TDP-glucose or UDP-glucose, and RmlT activity was quantified by measuring released phosphate over time. As before, activity detected with TDP-rhamnose was much higher than with the other nucleotides (Figure 5E). We then measured RmlT activity in a reaction containing equal

amounts of TDP-rhamnose and TDP-glucose. If specificity is thermodynamically determined in the ternary complex, then the rate of the reaction should not change much with the addition of TDP-glucose since most of the ternary complexes will contain TDP-rhamnose. However, if the two donor nucleotides bind equally well and specificity is kinetically determined, we should observe a clear reduction in the rate of reaction, since only the fraction of the ternary complexes with bound TDP-rhamnose would result in donor hydrolysis. The time course of the TDP-rhamnose/TDP-glucose mixture showed a clear decrease in the initial activity rate calculated from the first 2 minutes, from 4.8 to 1.4 μM phosphate released/min/μM RmlT (Figure 5E). Moreover, when RmlT was incubated with mixed TDP-rhamnose and UDP-glucose (which binds very weakly to RmlT), the reaction occurred as in the presence of only TDP-rhamnose. In summary, these results support the proposal that RmlT specificity is kinetically determined.

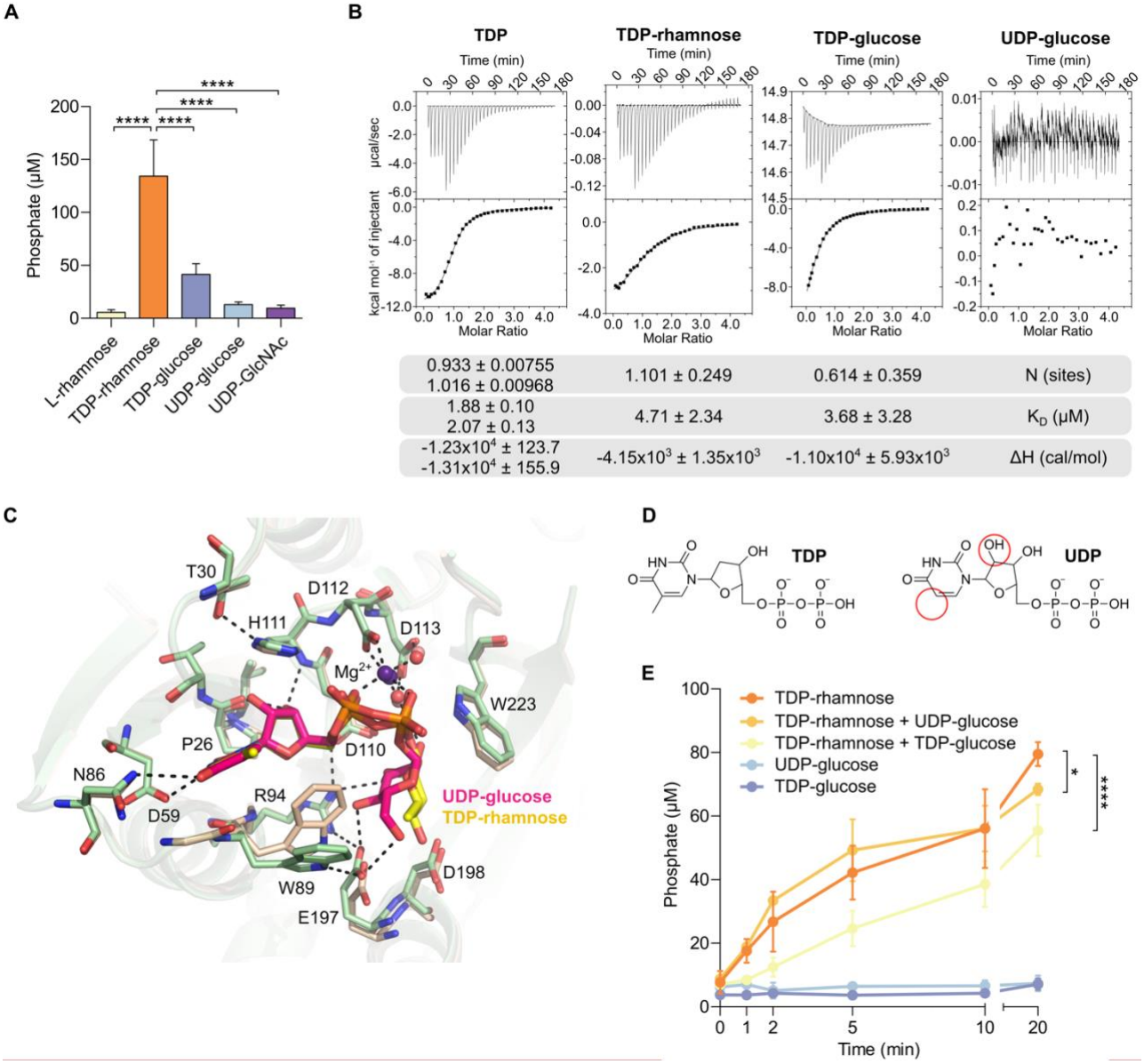

Figure 5: Donor substrate selectivity in RmlT. A) Purified recombinant RmlT (2 µM) was incubated with 1mM WTA and 200 µM TDP-rhamnose, L-rhamnose, TDP-glucose, UDP-glucose or UDP-GlcNAc. RmlT activity was measured after 30 minutes by quantifying released phosphate. B) ITC measurement of RmlT/donor substrate interactions. Upper panels show the titration of RmlT with TDP-rhamnose, TDP-glucose, TDP or UDP-glucose. The lower panel shows heat released when substrate binds to RmlT as a function of relative concentrations. Corrections due to dilution have been made to heat released. Solid lines correspond to the best fit of data using a bimolecular interaction model. Table shows N-value (commonly referred as the stoichiometry), binding constant K_D (µM) and reaction enthalpy (ΔH) extracted from model fitting. Values are mean ± SD (n = 3, except for the values of TDP which n=2 and both replicates are displayed). C) Superposition of the active-sites of RmlT/UDP-glucose (green with UDP-glucose in pink, PDB code: 8BZ6) and RmlT/TDP-rhamnose (wheat with TDP-rhamnose in yellow, PDB code: 8BZ7) with the substrate-interacting residues as sticks. Hydrogen bonds between RmlT residues and UDP-glucose are represented as black dashed lines. Water and Mg^{2+} are shown as red and purple spheres, respectively. D) Chemical structure of TDP (left) and UDP (right) with differences highlighted by red circles. E) Time-dependent activity of RmlT with different donor substrates by quantification of released phosphate. Reactions contained 1 mM WTA, 200 µM of each nucleotide and 2 µM RmlT. Values are the mean

± SD (n = 3, except for the curve of TDP-glucose in which n = 4). *p*-values were calculated using a two-way ANOVA; * $p < 0.05$, **** $p < 0.0001$.

RmlT rhamnosylates naked WTA

We also wondered if RmlT displays specificity towards WTA modifications, in particular WTA glycosylations. We thus analysed RmlT activity in the presence of TDP-rhamnose and WTA purified from wild-type EGDe strain and isogenic mutants presenting different glycosylation patterns: decorated with rhamnose at position *C*-4 and GlcNAc at *C*-2 of the ribitol-phosphate units (isolated from wild-type *L. monocytogenes* EGDe strain), decorated only with GlcNAc (isolated from the EGDe Δ*rmlT* strain), decorated only with rhamnose (isolated from the EGDe Δ*lmo1079* strain), or without any decoration (naked WTA) isolated from the EGDe Δ*rmlTΔlmo1079* strain. While some RmlT activity was detected with rhamnose-decorated WTA, suggesting incomplete glycosylation at *C*-4, clearly the strongest activity of RmlT was detected in the presence of naked WTA (Figure 6A). Importantly, no activity was observed with WTA containing only GlcNAc, indicating that the presence of GlcNAc impairs RmlT activity and strongly suggesting that in the bacterial cell, RmlT likely functions before the glycosyltransferase (Lmo1079) that adds GlcNAc on WTA.

We also analysed the electrostatic surface of RmlT structures looking for clues of where the negatively charged polymeric ribitol-phosphate binds. The surface shows a strongly positively charged groove that starts at the active site and runs along the interface between the catalytic and helical subdomains and into the tunnel delimited by the catalytic, helical and oligomerization subdomains (Figure 6B). In the high-resolution apo-structure, a HEPES molecule that includes a negatively-charged sulphonic acid group is present in this positively charged groove in all 4 asymmetric unit copies, while other HEPES molecules are observed in some but not all copies. Importantly, superposition of the RmlT structure with TarP bound to a 3- or 5-units of ribitol-phosphate (PDB codes: 6H4M, 6HNQ and 6H4F) shows the polymer sitting in the groove, running from the active site, close to the sugar and residue D198, into the tunnel (Figure 6C). This observation raised the question of how does a long WTA polymer enter the tunnel, leading to the hypothesis that, like in TarS, the oligomerization domain of RmlT can adopt different positions relative to the catalytic domain so that there is a closed conformation, corresponding to the crystallographic structure, and an open conformation that allows access of the WTA polymer to its binding groove and the tunnel.

To explore this hypothesis, we generated a metal bridge across the catalytic/oligomerization interface by mutating two residues that are in close proximity to cysteine (W145 on the catalytic subdomain

and A472 on the oligomerization subdomain) (Figure 6C) and performed the rhamnosylation reaction in the absence and presence of cadmium. Cadmium coordination by the two cysteines will bridge the two subdomains and stabilize the interface. If a transition between the closed and open conformations is important for the rhamnosylation reaction of WTA, then formation of the metal bridge will reduce activity. The mutant protein functioned as well as wild-type RmlT in the absence of cadmium cation, and the addition of 100 µM of $CdCl_2$ had no impact the activity of wild-type RmlT. However, Cd^{2+} reduced the activity of the mutant protein by more than 50 % (Figure 6D), supporting the importance of the transition between a closed and an open conformation for RmlT activity.

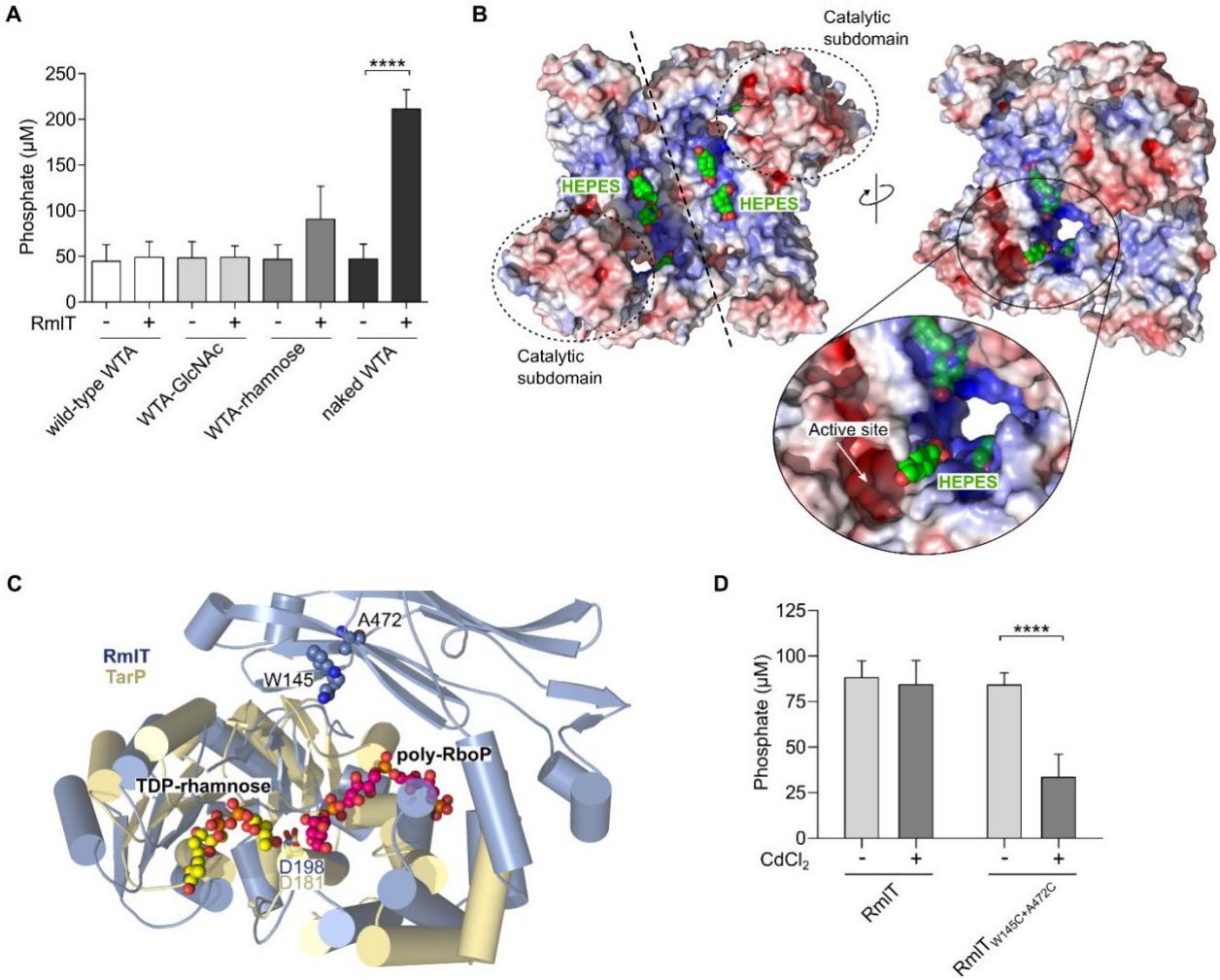

Figure 6: Properties of WTA as acceptor substrate. A) Quantification of phosphate released from the TDP generated by RmlT in presence of differently decorated WTA: wild-type WTA, containing both GlcNAc and rhamnose modifications (wild-type WTA purified from the *L. monocytogenes* strains EGDe); WTA containing only GlcNAc modification (WTA-GlcNAc purified from EGDe Δ*rmlT*); WTA containing only rhamnose modification (WTA-rhamnose purified from EGDe Δ*lmo1079*); and naked WTA without any glycosylation (naked WTA purified from EGDe Δ*rmlT*Δ*lmo1079*). Reaction mixtures included 5 mM WTA, 1 mM TDP-rhamnose and 10 µM RmlT incubated during 30 min. Values are

mean ± SD (n = 3); using one-way ANOVA, **** = $p < 0.0001$. B) Surface representation of RmlT colored according to the electrostatic potential [-8 kT/e (red) to 8kT/e (blue)]. Left and right panel are related by rotation. HEPES molecules are represented as sticks. Loop-C is hidden. Close-up view of the active site showing a HEPES molecule. C) Superposition of RmlT (blue, PDB code: 8BZ7) and TarP (yellow, PDB code: 6H4F) superposed at the active site region. TDP-rhamnose in the active site of RmlT and polymeric ribitol-phosphate (poly-RboP) bound to TarP are represented as spheres. D198 (RmlT numbering) and D181 (TarP numbering) are located between TDP-rhamnose and poly-RboP. RmlT W145 and A472 (mutated to cysteine) are represented as spheres. D) Quantification of phosphate released from the TDP generated by RmlT or $RmlT_{W145C+A472C}$ incubated with naked WTA and TDP-rhamnose in the presence of 100 µM of $CdCl_2$, during 30 min. Values are the mean ± SD (n = 4). *p*-values were calculated using a two-way ANOVA; **** $p < 0.0001$.

RmlT as new target for innovative anti-virulence approaches

RmlT is a bacteria-specific glycosyltransferase that, whereas not affecting bacterial fitness, is required for virulence and antimicrobial resistance [13, 14, 16, 17], thus appearing as a promising target for an innovative anti-virulence strategy against *L. monocytogenes*.

As a proof of concept, we assessed the impact on *in vivo* infection of the single mutation D198A that renders RmlT inactive but does not affect expression levels or solubility relative to wild-type RmlT when expressed in *E. coli*. Mice were intravenously infected with *L. monocytogenes* EGDe Δ*rmlT* or with the corresponding complemented strains expressing the wild-type RmlT (EGDe Δ*rmlT::rmlT*) or the $RmlT_{D198A}$ mutant (EGDe Δ$rmlT::rmlT_{D198A}$). Bacterial load per spleen and liver was assessed 72 h post-infection (Figure 7). Compared to the number of bacteria present in organs of animals infected with the *L. monocytogenes* EGDe Δ*rmlT* strain, the complementation with wild-type RmlT (EGDe Δ*rmlT::rmlT*) induced a significant increase in the number of bacteria present in both organs analyzed, restoring full bacterial virulence [13]. In contrast, complementation with the inactive RmlT variant (EGDe Δ$rmlT::rmlT_{D198A}$) did not increase the number of bacteria present in the organs of infected mice. These results indicate that inactivation of RmlT by a single mutation in its active site generates attenuated bacteria, supporting RmlT as a potential target for new anti-virulence approaches.

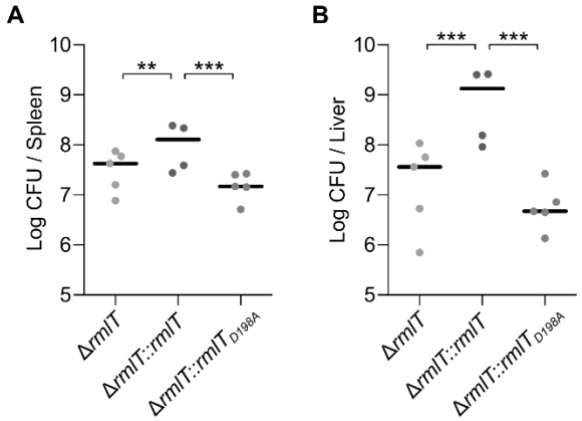

Figure 7: Impact of RmlT activity in the ability of *L. monocytogenes* to infect mice. Bacterial counts in the spleens (A) and livers (B) of the mice 72h after intravenous inoculation of the *L. monocytogenes* strains EGDe Δ*rmlT*, EGDe Δ*rmlT*::*rmlT* or EGDe Δ*rmlT*::*rmlT*$_{D198A}$. Data are presented as scatter plots, with the counts for each animal indicated by dots and the mean by a horizontal line (n = 5, except for EGDe Δ*rmlT*::*rmlT* in which n = 4). The *p*-value was calculated using a one-way ANOVA; ** $p < 0.01$, *** $p < 0.001$.

Discussion

Glycosylation of WTA from Gram-positive pathogens is crucial for bacterial virulence and resistance to antimicrobials. Despite the significant impact of WTA glycosyltransferases on crucial aspects of bacterial infection, identification and characterization of these enzymes, which represent promising target for novel anti-virulence strategies, has been limited. In this study, we have elucidated the first structure and uncovered functional details of a bacterial WTA rhamnosyltransferase, RmlT, expressed by the major Gram-positive foodborne pathogen *L. monocytogenes*. Structural analysis of RmlT reveals strong similarities with the structure of *S. aureus* glycosyltransferase TarS, both sharing the same tertiary organization in the catalytic, helical, oligomerization and turret subdomains. The catalytic and helical subdomains of these proteins are also identical in a third glycosyltransferase, *S. aureus* TarP. In addition, many of the residues present in the active site of RmlT are conserved in TarS and TarP. The most striking difference is that RmlT assembles as a dimer while TarS and TarP form trimers. We showed that the dimer interface is important for the physiological function of RmlT since mutations on the interface designed to disrupt the dimer architecture led to changes in protein stability *in vitro* and in the rhamnosylation pattern of the bacterial surface *in vivo*.

Although we have previously demonstrated that in *L. monocytogenes* the gene coding for RmlT is required for the decoration of WTA with rhamnose [13], the activity of the enzyme had never been characterized. We now have shown, using two different assays, that RmlT in the presence of TDP-rhamnose and naked WTA alters the electrophoretic mobility of WTA in a native-PAGE and releases TDP, consistent with the transfer of rhamnose from the donor substrate to WTA. Given the high

conservation of the catalytic residues across different WTA glycosyltransferases, we wondered what drives the specificity of RmlT activity for TDP-rhamnose. Using a combination of approaches, we showed that RmlT binds equally well to TDP-rhamnose and TDP-glucose but only transfers rhamnose to WTA and that this specificity is kinetically determined. Similar results were reported for *B. subtilis* TagA, a teichoic acid glycosyltransferase. TagA binds both UDP-*N*-acetylmannosamine (UDP-ManNAc) and UDP-GlcNAc but is enzymatically active only with UDP-ManNAc [30]. This finding raises the question of how the efficiency of WTA rhamnosylation is ensured in bacteria since other TDP coupled sugars will compete for the TDP-rhamnose binding site, slowing the production of decorated WTA. In addition, we showed that RmlT displays specificity for WTA, glycosylating WTA that lacks both rhamnose and GlcNAc [22, 27, 31, 32].

We could not clarify the specific role of the catalytic residues E197 and D198. D198 aligns with the proposed catalytic residue in *S. aureus* Tar proteins, and E197 is involved in substrate binding in these glycosyltransferases [24, 27]. In RmlT, E197 interacts with the sugar but when we mutated D198 to alanine the sugar moved away from the catalytic pocket. Thus, E197 alone is not able to stabilize the sugar in a catalytically competent position. Despite the ambiguity, it is clear from the structures that D198 is better positioned to activate the ribitol for nucleophilic attack.

Overall, our data provides a novel insight into the molecular mechanism of WTA glycosyltransferases. Through comparison between the structures of RmlT and TarS and biochemical crosslinking across the interface between the RmlT catalytic and oligomerization subdomains, we propose that RmlT undergoes a transition between an open conformation, where the catalytic-oligomerization interface is not established and the WTA polymer can bind to the protein, and a closed conformation, where the interface is formed and the polymer is trapped inside the tunnel formed by the catalytic, oligomerization and helical subdomains. Interestingly, the closed conformation should increase the lifetime of the enzyme-WTA complex, favoring processivity of the enzyme as proposed for TarS and TarP (Figure 8) [24, 27].

By combining our findings with earlier discoveries, we clarified several stages of WTA glycosylation in *L. monocytogenes* serovar 1/2a. In particular, our data supports that the newly formed WTA is first decorated with rhamnose by RmlT. This indicates that decoration with GlcNAc by Lmo1079 follows rhamnosylation, fitting well with the physiological location of RmlT in the cytosol and of Lm1079 on the external surface of the plasma membrane (Figure 8). We also suggest that rhamnosylation (step 1) involves trapping of WTA by the RmlT molecule, favoring multiple cycles of rhamnosylation before release of the decorated WTA. Flipping of the rhamnosylated WTA to the outside of the cell membrane (step 2) is likely to result from the action of a homolog of the *S. aureus* TarGH ABC

transporter (predicted to be Lmo1074-75) [33, 34]. In parallel, it has been proposed that the cytoplasmic glycosyltransferase Lmo2550 uses UDP-GlcNAc to form a C_{55}-P-GlcNAc WTA intermediate that is also flipped across the membrane by the flippase GtcA [29]. The membrane-associated glycosyltransferase Lmo1079 then transfers the GlcNAc moiety to the rhamnosylated-WTA backbone on the outside of the cell [35, 36]. (step 3). Finally, the mature WTA is transferred to the bacterial cell wall by a still unclear mechanism proposed to be promoted in *S. aureus* by the TarTUV enzymes (step 4) [31].

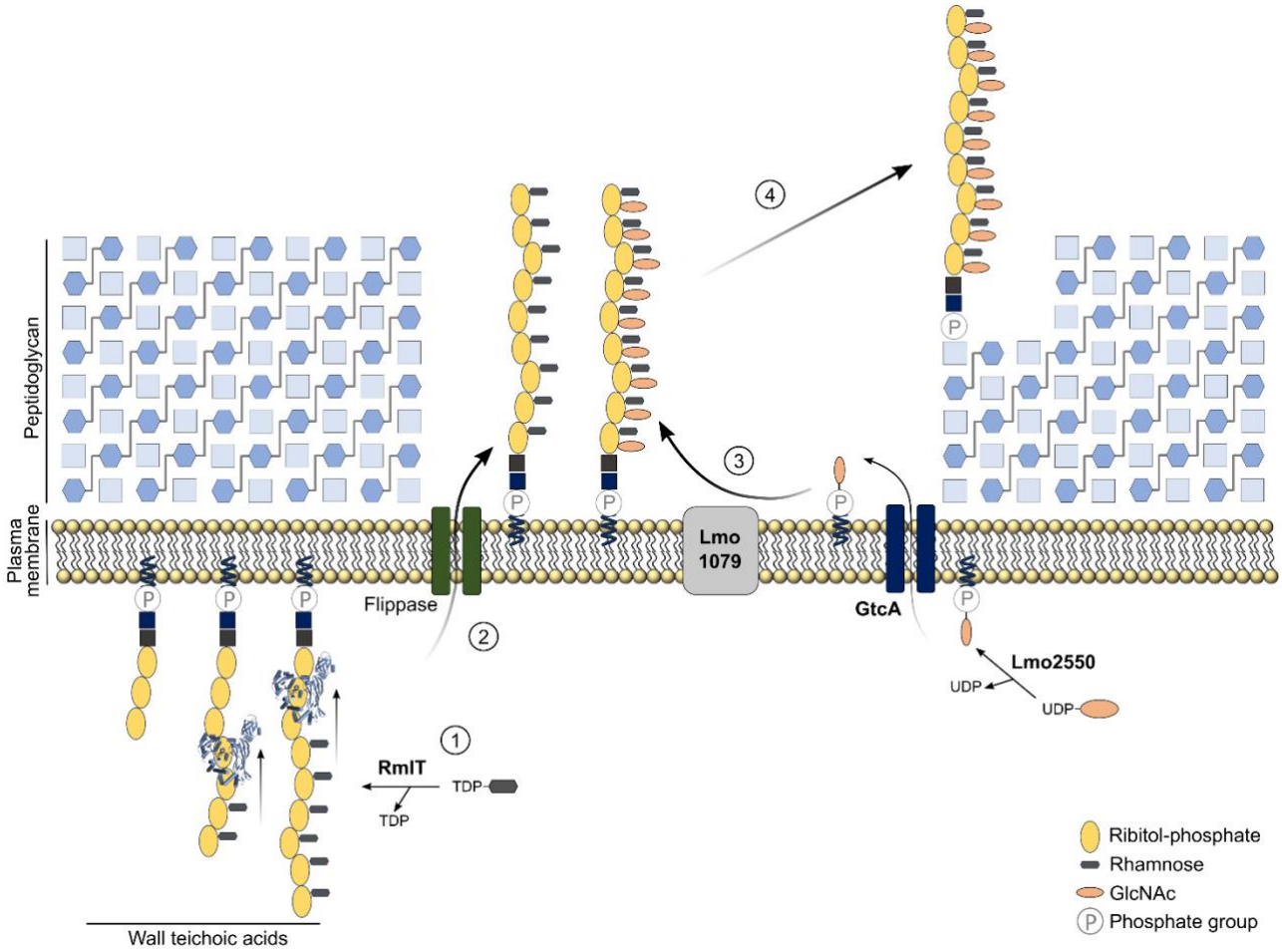

Figure 8: Proposed model for the glycosylation of WTA in *L. monocytogenes* EGDe serovar 1/2a. Step 1: In the cytoplasm, RmlT decorates newly formed chains of ribitol-phosphate with rhamnose units from TDP-rhamnose. Step 2: Rhamnosylated WTA are flipped across the membrane, probably by the Lmo1074-75 complex, homolog to the *S. aureus* two-component ATP-binding cassette (ABC) transporter TarGH. Step 3: Rhamnosylated WTA are glycosylated by Lmo1079 with GlcNAc from a C_{55}-P-GlcNAc intermediate previously formed by the cytoplasmic glycosyltransferase Lmo2550 using UDP-GlcNAc and then flipped across the membrane by the GtcA flippase. Step 4: Fully decorated WTA are anchored to the cell wall, possibly by a homolog of the *S. aureus* TarTUV complex.

In summary, WTA glycosylations are involved in many bacterial features across different species including bacterial virulence [13, 14], resistance to antibiotics [16, 23, 25, 37-40] and antimicrobial peptides [13] and in the localization of important surface proteins that facilitate host immune evasion and colonization [23, 25, 37, 38]. Therefore, it is tempting to consider glycosylation of bacterial WTA as a conserved virulence mechanism in Gram-positive pathogens. Importantly, our experiments proved that mutation of a single residue in the active site of RmlT leads to enzyme inactivation and to a significant decrease in the capacity of *L. monocytogenes* cells to infect mice. Together with the relatively weak binding selectivity for TDP-modified molecules, this indicates that RmlT is a valid target for the development of next-generation antibacterial drugs that, by inhibiting specific sugar decorations, will not directly kill bacteria but will diminish bacterial virulence, increase susceptibility to host innate defences and potentiate the action of antibiotics while preserving the microbiota.

Methods

Cloning

rmlT was cloned into the expression vector pET28b by the polymerase incomplete primer extension (PIPE) method [41]. Briefly, *rmlT* was amplified by PCR from the *L. monocytogenes* EGDe (ATCC-BAA-679) genomic DNA, using the primers #1 and #2. The vector pET28b was also amplified by PCR using the primers #3 and #4. Both reactions generated a mixture of incomplete extensions products that contained short overlapping sequences at the ends, allowing the annealing of the complementary strands to produce hybrid vector-insert combinations. Vectors and primer sequences are presented in Supplementary Table 1-2, respectively.

Site-directed mutagenesis

The vectors pET28b-*rmlT*$_{D198A}$, pET28b-*rmlT*$_{E197A}$, pET28b-*rmlT*$_{W89A}$, pET28b-*rmlT*$_{W223A}$, pET28b-*rmlT*$_{Y368A+E372A}$, pET28b-*rmlT*$_{Y347A+Y368A+E372A}$, pET28b-*rmlT*$_{W145C+A472C}$, pPL2-*rmlT*$_{D198A}$, pPL2-*rmlT*$_{E197A}$, pPL2-*rmlT*$_{W89A}$, pPL2-*rmlT*$_{W223A}$, pPL2-*rmlT*$_{Y368A+E372A}$ and pPL2-*rmlT*$_{Y347A+Y368A+E372A}$ were obtained by site-directed mutations using pET28b-*rmlT* or pPL2-*rmlT* [13] as templates and the primer pairs #5 and #6 (for pET28b-*rmlT*$_{D198A}$ and pPL2-*rmlT*$_{D198A}$), #7 and #8 (for pET28b-*rmlT*$_{E197A}$ and pPL2-*rmlT*$_{E197A}$), #9 and #10 (for pET28b-*rmlT*$_{W89A}$ and pPL2-*rmlT*$_{W89A}$), #11 and #12 (for pET28b-*rmlT*$_{W223A}$ and pPL2-*rmlT*$_{W223A}$), #13 and #14 (for pET28b-*rmlT*$_{Y368A+E372A}$ and pPL2-*rmlT*$_{Y368A+E372A}$), #13, #14 #15 and #16 (for pET28b-*rmlT*$_{Y347A+Y368A+E372A}$ and pPL2-*rmlT*$_{Y347A+Y368A+E372A}$) and #17, #18, #19, #20 (for pET28b-*rmlT*$_{W145C+A472C}$). Primer information is presented in Supplementary Table 2. Mutations were confirmed by sequencing.

Expression and purification of RmlT variants

Escherichia coli BL21(DE3) cells transformed with pET28b coding for N-terminally hexahistidine tagged RmlT (pET28b-*rmlT*), RmlT$_{D198A}$ (pET28b-*rmlT*$_{D198A}$), RmlT$_{E197A}$ (pET28b-*rmlT*$_{E197A}$), RmlT$_{W89A}$ (pET28b-*rmlT*$_{W89A}$), RmlT$_{W223A}$ (pET28b-*rmlT*$_{W223A}$), RmlT$_{Y368A+E372A}$ (pET28b-*rmlT* $_{Y368A+E372A}$), RmlT$_{Y347A+Y368A+E372A}$ (pET28b-*rmlT* $_{Y347A+Y368A+E372A}$) or RmlT$_{W145C+A472C}$ (pET28b-*rmlT* $_{W145C+A472C}$) were grown in LB supplemented with 30 μg ml^{-1} kanamycin at 37°C for 3 h. Protein expression was induced with 0.5 mM isopropyl β-D-1-thiogalactopyranoside (IPTG). After 16 h-growth at 30°C, cells were harvested, resuspended in lysis buffer (50 mM NaH_2PO_4 pH 8.0, 300 mM NaCl, 10 mM

Imidazole) and lysed by sonication. Cell lysate was clarified by centrifugation and incubated with an immobilized metal-affinity matrix (Ni-NTA Agarose, ABT Technologies), pre-equilibrated with lysis buffer, at 4 °C for 1 h. After washing the column with 50 mM NaH_2PO_4 pH 8.0, 300 mM NaCl, 30-50 mM Imidazole, proteins were eluted with 50 mM NaH_2PO_4, 300 mM NaCl, pH 8.0, 100-300 mM Imidazole. Eluted material was concentrated using a 30 kDa cut-off membrane concentrator (Vivaspin, Sartorius Stedim Biotech) concomitantly with buffer exchange to 20 mM Tris-HCl pH 8.0, 100 mM NaCl, 1 mM DTT. Hexahistidine tag (His-tag) was removed by digestion with TEV protease (1:10 molar ratio) at 4 °C for 16 h. Proteins were separated from TEV protease, His-tag and uncut proteins by a second immobilized metal-affinity column pre-equilibrated with storage buffer (20 mM Tris-HCl pH 8.0, 100 mM NaCl, 1 mM DTT). Flow-through containing the untagged proteins was concentrated and loaded into a Superdex-200 10/300 GL column (GE Healthcare) pre-equilibrated with storage buffer. Fractions containing pure proteins were pooled and concentrated. Protein concentration was estimated by measuring absorbance at 280 nm and using extinction coefficients calculated with the ExPASY tool Protparam. Purified RmlT variants were flash-frozen in liquid nitrogen and stored at -80 °C.

Expression and purification of selenomethionine-containing RmlT variant

E. coli B834(DE3) cells transformed with pET28b-*rmlT* were grown in 20 mL LB medium overnight at 37 °C. Cells were collected, washed three times with sterile deionized water and used to inoculate SelenoMethionine medium (Molecular Dimensions). Protein expression and purification was performed as described in the previous section.

Crystallization of RmlT variants

Initial crystallization conditions for RmlT were determined at 20°C using commercial sparse-matrix crystallization screens. Sitting-drop vapor diffusion experiments were set up in 96-well CrystalQuick plates using an Oryx 4 crystallization robot (Douglas Instruments). Drops consisted of equal volumes (0.3 µL) of RmlT protein solution (at 10 mg mL^{-1} in 20 mM Tris-HCl pH 8.0, 100 mM NaCl, 1 mM DTT) and crystallization solutions, equilibrated against 40 µL reservoir solution. The apo RmlT structure with bound HEPES was obtained from a crystal grown in solution B9 from JBScreen Wizard 1 & 2 crystallization screen [100 mM HEPES-NaOH pH 7.5, 20 % (w/v) PEG 8,000]. This crystal was frozen directly in liquid nitrogen. Selenomethionine-containing crystals (apo structure) were first obtained in solution H5 from NeXtal Cystal Classic II Suite crystallization screen (100 mM succinic acid pH 7.0, 15 % (w/v)

PEG 3,350). Crystals were reproduced using MRC Maxi 48 well plates with drops composed of equal volumes (1 µL) of protein (at 10 mg mL^{-1} in 20 mM Tris-HCl pH 8.0, 100 mM NaCl, 1 mM DTT) and crystallization solution (200 mM succinic acid pH 7.0, 10 % (w/v) PEG 3,350) equilibrated against 150 µL reservoir. Crystals were cryo-protected with a 1:1 mixture of Paratone N and Mineral oil before being frozen in liquid nitrogen. RmlT crystals were also obtained in condition F9 from PACT premier (Molecular Dimensions) [100 mM Bis-Tris proprane pH 6.5, 200 mM K/Na tartrate tetrahydrate, 20 % PEG 3,350] and were optimized by varying pH and concentration of PEG 3,350, using a 1 µL:1 µL drop ratio of protein to crystallization solution equilibrated against 150 µL reservoir solution. RmlT/TDPrhamnose structure was determined from soaking a crystal obtained in 100 mM Bis-Tris Propane pH 7.0, 200 mM K/Na tartrate tetrahydrate, 20 % (w/v) PEG 3,350. Before freezing, 0.5 µL of a solution containing 55 mM Bis-Tris propane pH 7.0, 110 mM K/Na tartrate tetrahydrate, 13.75 % (w/v) PEG 3,350, 5 % (v/v) glycerol, 25 mM $MgCl_2$ and 30 mM TDP-rhamnose was added and the drop was allowed to equilibrate for 50 min. After quickly transferring the crystal into a solution containing 220 mM K/Na tartrate tetrahydrate, 110 mM Bis-Tris propane pH 7.0, 27.5 % (w/v) PEG 3,350, 10 % (v/v) glycerol, the crystal was flash-frozen in liquid nitrogen. The structure of $RmlT_{D198A}$ in complex with TDP-rhamnose was determined from a crystal grown in 100 mM Bis-Tris propane pH 7.0, 200 mM K/Na tartrate, 22.5 % (w/v) PEG 3,350. Crystal was transferred to a 0.5 µL of reservoir solution and then 0.5 µL of 55 mM Bis-Tris propane pH 7.0, 110 mM K/Na tartrate tetrahydrate, 16.75 % (w/v) PEG 3,350, 20 mM $MgCl_2$, 20 mM TDP-rhamnose was added. The mixture was allowed to equilibrate for 6 min. Cryoprotection was achieved by adding 0.8 µL of a solution containing 110 mM Bis-Tris propane pH 7.0, 220 mM K/Na tartrate tetrahydrate, 33.5 % (w/v) PEG 3,350 prior to flash-freeze in liquid nitrogen. Finally, RmlT crystals were also obtained in the condition H6 of the NeXtal Classics Lite Suite crystallization screen (100 mM Tris-HCl pH 8.5, 200 mM sodium acetate., 15 % (w/v) PEG 4,000). A crystal grown in this condition was used to solve the RmlT/UDP-glucose structure. Crystal was sequentially transferred to solutions with increasing concentration of DMSO and supplemented with UDP-glucose (110 mM Tris-HCl pH 8.5, 220 mM sodium acetate, 16.5 % (w/v) PEG 4,000, 10 to 30 % DMSO, 5 mM MgCl2, 5 mM UDP-glucose) before flash-freezing in liquid nitrogen.

Data collection and processing

Diffraction data were collected from cryo-cooled (100 K) single crystals at ~0.98 Å and at beamlines PROXIMA-1 and PROXIMA-2A of the French National Synchrotron Facility

(SOLEIL, Gif-sur-Yvette, France) and XALOC of ALBA (Barcelona, Spain). Data sets were processed with XDS [42] and reduced with utilities from the CCP4 program suite [43]. X-ray diffraction data collection and processing are summarized in Supplementary Table 3.

Structure determination, model building and refinement

The structure of apo RmlT was solved by single-wavelength anomalous diffraction (SAD), using the anomalous signal of the selenium at the *K*-absorption edge and pipelines from CCP4 package [43]: the SHELXC/SHELXD/SHELXE pipeline [44] was used for Se atom location, the Phaser SAD pipeline [45, 46] was for density modification and automatic model building and the Buccaneer pipeline [47, 48] used for automatic model building and refinement. All the other structures were solved by molecular replacement with Phaser [45] using the chain A of the apo structure as a search model. Alternating cycles of model building with Coot [49] and refinement with PHENIX [50] were performed until model completion. Refined coordinates and structure factors were deposited at the Protein Data Bank [51]. The PDB accession codes 8BZ4, 8BZ5, 8BZ6, 8BZ7 and 8BZ8 were assigned to apo RmlT, apo RmlT with HEPES, RmlT in complex with UDP-glucose, RmlT in complex with TDP-rhamnose, and $RmlT_{D198A}$ in complex with TDP-rhamnose, respectively. Refinement statistics are summarized in Supplementary Table 3.

Isothermal titration calorimetry

Recombinant RmlT was dialysed overnight against 20 mM HEPES pH 8.0, 100 mM NaCl, 5 mM $MgCl_2$. Solution of 200 µM TDP, TDP-rhamnose, TDP-glucose or UDP-glucose (calorimetric syringe) were titrated into 20 µM RmlT (sample cell), with an initial injection of 2 µL, followed by 28 injections of 10 µL. Titrations were performed in a MicroCal VP-ITC instrument (GE Healthcare) at 15 °C. Data were visualized and analyzed with Origin 7 Software using a single-site binding model.

Analytical size-exclusion chromatography

Analytical size-exclusion chromatography was performed on a Superdex 200 10/300 GL column (GE Healthcare) pre-equilibrated with storage buffer. Blue dextran (2,000 kDa), Ferritin (440 kDa), Aldolase (158 kDa), Ovalbumin (43 kDa) and Ribonuclease A (13.7 kDa) were used as standards for column calibration. The K_{av} *versus* Log molecular weight was calculated using the equation $K_{av} = (V_e - V_0)/(V_t - V_0)$, where V_e is the elution volume of the protein, V_0 is the void volume of the column and V_t is the column bed volume.

***Listeria monocytogenes* strains**

We previously generated the *L. monocytogenes* strains EGDe Δ*rmlT*, EGDe Δ*rmlT*::*rmlT* [13] and EGDe Δ*rmlT*Δ*lmo1079* [16]. To generate the *L. monocytogenes* strains EGDe Δ*rmlT*::*rmlT*$_{D198A}$, EGDe Δ*rmlT*::*rmlT*$_{E197A}$, EGDe Δ*rmlT*::*rmlT*$_{W89A}$, EGDe Δ*rmlT*::*rmlT*$_{W223A}$, EGDe Δ*rmlT*::*rmlT*$_{Y368A+E372A}$ and EGDe Δ*rmlT*::*rmlT*$_{Y347A+Y368A+E372A}$ strains, the pPL2-derivative plasmids described above were introduced into *E. coli* S17–1 and transferred to the *L. monocytogenes* EGDe Δ*rmlT* strain by conjugation on Brain Heart Infusion (BHI) agar. Transconjugant clones were selected in BHI supplemented with chloramphenicol/ colistin/nalidixic acid (Cm/Col/Nax) and chromosomal integration of the plasmids confirmed by PCR and sequencing.

Isolation and purification of wall teichoic acids

Wall teichoic acids (WTA) from *L. monocytogenes* strains wild-type, Δ*rmlT*, Δ*lmo1079* and Δ*rmlT*Δ*lmo1079*, were isolated and purified as previously described [52] with some modifications. *L. monocytogenes* cells grown overnight in 20 mL BHI at 37 °C were collected by centrifugation at 4,000 xg for 10 min. The cells were washed once in buffer 1 (50 mM MES pH 6.5), resuspended in buffer 2 (50 mM MES pH 6.5, 4 % (w/v) SDS), and boiled in a water bath for 1 h. Cell debris was collected by centrifugation at 4,000 xg for 10 min and resuspended in 2 mL of buffer 1. The pellet was washed sequentially in 1 ml of buffers 2, 3 [50 mM MES pH 6.5, 2 % (w/v) NaCl] and 1. Washed pellet was resuspended in 1 mL of 20 mM Tris-HCl pH 8.0, 0.5 % (w/v) SDS, 20 µg proteinase K and incubated at 50 °C for 4 h with agitation (1,400 rpm). To remove SDS, the sample was centrifuged at 16,000 xg for 1 min and washed once with buffer 3 and three times with distilled H_2O. Sample was then resuspended in 1 mL of 0.1 M NaOH and shaken at room temperature for 16 h. The remaining insoluble cell debris was removed by centrifugation at 16,000 xg for 10 min and the supernatant containing the hydrolyzed crude WTA was neutralized with 1 M Tris-HCl pH 7.8. The sample was dialyzed against distilled H_2O using a 1 kDa cut-off membrane. Finally, isolated crude WTAs were lyophilized and resuspended in ultra-pure H_2O to a final concentration of 10 mg mL^{-1} (considering ribitol monomer molecular weight) [52].

RmlT activity assay

The activity of RmlT variants was analyzed using the Glycosyltransferase Activity Kit (R&D Systems) according to the manufacturer's protocol. Recombinant RmlT (2 μM), was incubated with wild-type WTA, containing both GlcNAc and rhamnose modifications (wild-type WTA purified from the *L. monocytogenes* strains EGDe); WTA containing only GlcNAc modification (WTA- GlcNAc purified from EGDe Δ*rmlT*); WTA containing only rhamnose modification (WTA-rhamnose purified from EGDe Δ*lmo1079*); and naked WTA without any glycosylation (naked WTA purified from EGDe Δ*rmlT*Δ*lmo1079*) (1 mM) and TDP-rhamnose, UDP-rhamnose or UDP-glucose (200 μM) in reaction buffer (5 mM $MgCl_2$, 25 mM Tris, 10 mM $CaCl_2$, pH 7.5) at 37 °C for 30 min. Regarding the metal bridge coordination assay using $RmlT_{W145C+A472C}$, the enzyme (2 μM) was incubated with naked WTA (1 mM) and TDP-rhamnose (200 μM) at in reaction buffer (5 mM $MgCl_2$, 25 mM Tris, 10 mM $CaCl_2$, 100 μM TCEP, pH 7.5) at 37 °C for 30 min, in presence of absence of $CdCl_2$ (100 μM). Free phosphate released upon hydrolysis of the TDP or UDP produced by RmlT was quantified by absorbance at 620 nm using a Synergy 2 multi-mode plate reader (BioTek, USA). RmlT reaction mixtures were also separated in 20 % polyacrylamide gels and WTA were stained with 1 mg mL^{-1} Alcian Blue solution after overnight incubation.

Cell wall rhamnose binding assay

Rhamnose present at the bacterial surface was quantified using a bacteriophage receptor binding protein (gp17) fused to GFP (gp17-GFP) (provided by M. Loessner, ETH Zurich). The assay was performed as described before [18]. Briefly, purified gp17-GFP was centrifuged at 30,000xg and 4°C for 1 h to remove protein aggregates. One milliliter of exponentially growing bacterial (OD_{600nm} = 0.5-0.6) cells were centrifuged and resuspended in 100 µL of PBS and incubated with 2.4 µg of gp17-GFP at room temperature for 20 min. Cells were washed three times with PBS and binding to the bacterial cell wall was visualized using a fluorescence microscope Olympus BX53 or quantified using a plate reader Synergy 2 (BioTek, USA).

Animal infections

Virulence studies were performed in mouse models of BALB/c strain. Infections were performed in six-to-eight week-old specific-pathogen-free females (n=5, except for EGDe Δ*rmlT*::*rmlT* in which n=4) as described [53]. Briefly, intravenous infections were performed through the tail vein with 10^4 CFU of bacteria in PBS. The infection was carried out for 72 h, at which point animals were euthanatized by general anaesthesia. The spleen and liver were

aseptically collected, homogenized in sterile PBS, and serial dilutions of the organ homogenates plated in BHI agar. Mice were maintained at the i3S animal facilities, in high efficiency particulate air (HEPA) filter-bearing cages under 12 h light cycles, and were given sterile chow and autoclaved water *ad libitum*. All the animal procedures were performed in agreement with the guidelines of the European Commission for the handling of laboratory animals (directive 2010/63/EU), with the Portuguese legislation for the use of animals for scientific purposes (Decreto-Lei 113/2013), and were approved by the i3S Animal Ethics Committee as well as by the Direcção Geral de Veterinária (the Portuguese authority for animal protection) under licenses 2017-06-30 015302 and 2023-04-05 006564.

Statistical analyses

Statistical analyses were calculated using the software Prism 9 (GraphPad Software). Unpaired two-tailed Student's t-test was used to compare the means of two groups; one-way ANOVA was used with Tukey's post-hoc test for pairwise comparison of means from more than two groups, or with Dunnett's post-hoc test for comparison of means relative to the mean of a control group. Differences with a calculated *p*-value above 0.05 were considered non-significant and statistically significant differences were noted as follows: * = $p < 0.05$; ** = $p < 0.01$; *** = $p < 0.001$; **** = p <0,0001.

Supplementary Materials: Supplementary Figure 1: Structure of *L. monocytogenes* RmlT and *S. aureus* TarS, TarP., Supplementary Figure 2: Properties of RmlT., Supplementary Figure 3: Electron density map of the donor substrates TDP-rhamnose and UDP-glucose in different forms of RmlT., Supplementary Figure 4: Active site of RmlT with TDP-rhamnose or UDP-glucose., Supplementary Figure 5: Active sites of RmlT, TarS and TarP., Supplementary Figure 6: Amino-acid sequence alignment of RmlT, TarS and TarP., Supplementary Table 1: Bacterial strains and plasmids., Supplementary Table 2: Primers sequences., and Supplementary Table 3. Data collection, phasing and refinement statistics.

Author's contributions: RM, JMC and DC conceptualize the overarching aims of the research study. RM, TC, RP, SS, JMC and DC conceived and designed the experiments. RM, TC and RP performed the experiments and data acquisition. RM, TC, RP, SS, JMC and DC analysed and interpreted the data. JMC and DC had management as well as coordination responsibility for the execution of the research work. RM, JMC and DC contributed to the acquisition of the

financial supports and resources leading to this publication. All authors contributed to the drafting of some parts of the manuscript, including reading and revising critically the manuscript for important intellectual content, as well as approval of the final version.

Competing interests: All authors have declared no competing interests.

Acknowledgments: The work leading to these results was supported by FEDER – "Fundo Europeu de Desenvolvimento Regional" funds through the NORTE 2020 - Norte Portugal Regional Operational Programme, Portugal 2020, and by Portuguese funds through FCT - Fundação para a Ciência e a Tecnologia/Ministério da Ciência, Tecnologia e Ensino Superior in the framework of the project NORTE-01-0145-FEDER-030020 and PTDC/SAU-INF/30020/2017, and by the "la Caixa" Foundation and FCT, I.P. under project CI21-00035 and LCF/PR/ HR23-00682.

The authors acknowledge the SOLEIL and ALBA synchrotrons for access and thank their staff for help with data collection. Support from the Biochemical and Biophysical Technologies, Animal Facility and X-ray Crystallography scientific platforms of i3S (Porto, Portugal) is also acknowledged. The authors extend their appreciation to Martin J. Loessner from ETH Zurich (Switzerland) that kindly provided the gp17-GFP recombinant construct.

References

1. ECDC, *Listeriosis*, in *ECDC. Annual Epidemiological Report*. 2023.
2. ECDC, *The European Union One Health 2021 Zoonoses Report.* 2022.
3. Brown, S., J.P. Santa Maria, Jr., and S. Walker, *Wall teichoic acids of gram-positive bacteria.* Annu Rev Microbiol, 2013. **67**: p. 313-36.
4. Sumrall, E.T., et al., *Structure and function of Listeria teichoic acids and their implications.* Molecular microbiology, 2020. **113**(3): p. 627-637.
5. Percy, M.G. and A. Grundling, *Lipoteichoic acid synthesis and function in gram-positive bacteria.* Annu Rev Microbiol, 2014. **68**: p. 81-100.
6. Rismondo, J., M.G. Percy, and A. Grundling, *Discovery of genes required for lipoteichoic acid glycosylation predicts two distinct mechanisms for wall teichoic acid glycosylation.* J Biol Chem, 2018. **293**(9): p. 3293-3306.
7. Percy, M.G., et al., *Identification of a Lipoteichoic Acid Glycosyltransferase Enzyme Reveals that GW-Domain-Containing Proteins Can Be Retained in the Cell Wall of Listeria monocytogenes in the Absence of Lipoteichoic Acid or Its Modifications.* J Bacteriol, 2016. **198**(15): p. 2029-42.
8. Uchikawa, K., I. Sekikawa, and I. Azuma, *Structural studies on lipoteichoic acids from four Listeria strains.* Journal of Bacteriology, 1986. **168**(1): p. 115-22.
9. Promadej, N., et al., *Cell wall teichoic acid glycosylation in Listeria monocytogenes serotype 4b requires gtcA, a novel, serogroup-specific gene.* Journal of Bacteriology, 1999. **181**(2): p. 418-25.
10. Swaminathan, B. and P. Gerner-Smidt, *The epidemiology of human listeriosis.* Microbes Infect, 2007. **9**(10): p. 1236-43.
11. Sumrall, E.T., et al., *Glycotyping and Specific Separation of Listeria monocytogenes with a Novel Bacteriophage Protein Tool Kit.* Applied and environmental microbiology, 2020. **86**(13).
12. Carvalho, F., S. Sousa, and D. Cabanes, *How Listeria monocytogenes organizes its surface for virulence.* Front Cell Infect Microbiol, 2014. **4**: p. 48.
13. Carvalho, F., et al., *L-Rhamnosylation of Listeria monocytogenes Wall Teichoic Acids Promotes Resistance to Antimicrobial Peptides by Delaying Interaction with the Membrane.* PLoS Pathog, 2015. **11**(5): p. e1004919.
14. Carvalho, F., S. Sousa, and D. Cabanes, *l-Rhamnosylation of wall teichoic acids promotes efficient surface association of Listeria monocytogenes virulence factors InlB and Ami through interaction with GW domains.* Environmental microbiology, 2018. **20**(11): p. 3941-3951.
15. Spears, P.A., et al., *Listeria monocytogenes wall teichoic acid decoration in virulence and cell-to-cell spread.* Mol Microbiol, 2016. **101**(5): p. 714-30.
16. Meireles, D., et al., *Listeria monocytogenes Wall Teichoic Acid Glycosylation Promotes Surface Anchoring of Virulence Factors, Resistance to Antimicrobial Peptides, and Decreased Susceptibility to Antibiotics*. Pathogens (Basel, Switzerland), 2020. **9**(4).
17. Sumrall, E.T., et al., *Phage resistance at the cost of virulence: Listeria monocytogenes serovar 4b requires galactosylated teichoic acids for InlB-mediated invasion.* PLoS pathogens, 2019. **15**(10): p. e1008032.
18. Bielmann, R., et al., *Receptor binding proteins of Listeria monocytogenes bacteriophages A118 and P35 recognize serovar-specific teichoic acids.* Virology, 2015. **477**: p. 110-118.

19. Faith, N., et al., *The role of L. monocytogenes serotype 4b gtcA in gastrointestinal listeriosis in A/J mice.* Foodborne Pathog Dis, 2009. **6**(1): p. 39-48.
20. Shen, Y., et al., *Structural and functional diversity in Listeria cell wall teichoic acids.* J Biol Chem, 2017. **292**(43): p. 17832-17844.
21. Cheng, Y., et al., *Teichoic acid glycosylation mediated by gtcA is required for phage adsorption and susceptibility of Listeria monocytogenes serotype 4b.* Applied & Environmental Microbiology, 2008. **74**(5): p. 1653-5.
22. Xia, G., et al., *Glycosylation of wall teichoic acid in Staphylococcus aureus by TarM.* J Biol Chem, 2010. **285**(18): p. 13405-15.
23. Brown, S., et al., *Methicillin resistance in Staphylococcus aureus requires glycosylated wall teichoic acids.* Proc Natl Acad Sci U S A, 2012. **109**(46): p. 18909-14.
24. Gerlach, D., et al., *Methicillin-resistant Staphylococcus aureus alters cell wall glycosylation to evade immunity.* Nature, 2018. **563**(7733): p. 705-709.
25. Guo, Y., et al., *Cell wall glycosylation in Staphylococcus aureus: targeting the tar glycosyltransferases.* Curr Opin Struct Biol, 2021. **68**: p. 166-174.
26. Sobhanifar, S., et al., *Structure and mechanism of Staphylococcus aureus TarM, the wall teichoic acid alpha-glycosyltransferase.* Proceedings of the National Academy of Sciences of the United States of America, 2015. **112**(6): p. E576-85.
27. Sobhanifar, S., et al., *Structure and Mechanism of Staphylococcus aureus TarS, the Wall Teichoic Acid beta-glycosyltransferase Involved in Methicillin Resistance.* PLoS pathogens, 2016. **12**(12): p. e1006067.
28. Camejo, A., et al., *In vivo transcriptional profiling of Listeria monocytogenes and mutagenesis identify new virulence factors involved in infection.* PLoS Pathog, 2009. **5**(5): p. e1000449.
29. Rismondo, J., et al., *GtcA is required for LTA glycosylation in Listeria monocytogenes serovar 1/2a and Bacillus subtilis.* Cell Surf, 2020. **6**: p. 100038.
30. Martinez, O.E., et al., *Insight into the molecular basis of substrate recognition by the wall teichoic acid glycosyltransferase TagA.* J Biol Chem, 2022. **298**(2): p. 101464.
31. van der Es, D., et al., *Teichoic acids: synthesis and applications.* Chemical Society Reviews, 2017. **46**(5): p. 1464-1482.
32. Winstel, V., G. Xia, and A. Peschel, *Pathways and roles of wall teichoic acid glycosylation in Staphylococcus aureus.* Int J Med Microbiol, 2014. **304**(3-4): p. 215-21.
33. Weidenmaier, C., et al., *Role of teichoic acids in Staphylococcus aureus nasal colonization, a major risk factor in nosocomial infections.* Nat Med, 2004. **10**(3): p. 243-5.
34. Brown, S., Y.H. Zhang, and S. Walker, *A revised pathway proposed for Staphylococcus aureus wall teichoic acid biosynthesis based on in vitro reconstitution of the intracellular steps.* Chem Biol, 2008. **15**(1): p. 12-21.
35. Eugster, M.R., et al., *Bacteriophage predation promotes serovar diversification in Listeria monocytogenes.* Mol Microbiol, 2015. **97**(1): p. 33-46.
36. Rismondo, J. and L.M. Schulz, *Not Just Transporters: Alternative Functions of ABC Transporters in Bacillus subtilis and Listeria monocytogenes.* Microorganisms, 2021. **9**(1).
37. Gerlach, D., et al., *Methicillin-resistant Staphylococcus aureus alters cell wall glycosylation to evade immunity.* Nature, 2018. **563**(7733): p. 705-709.
38. Hort, M., et al., *The Role of beta-Glycosylated Wall Teichoic Acids in the Reduction of Vancomycin Susceptibility in Vancomycin-Intermediate Staphylococcus aureus.* Microbiol Spectr, 2021. **9**(2): p. e0052821.

39. Smith, R.E., et al., *Decoration of the enterococcal polysaccharide antigen EPA is essential for virulence, cell surface charge and interaction with effectors of the innate immune system.* PLoS pathogens, 2019. **15**(5): p. e1007730.
40. Dale, J.L., et al., *Multiple roles for Enterococcus faecalis glycosyltransferases in biofilm-associated antibiotic resistance, cell envelope integrity, and conjugative transfer.* Antimicrob Agents Chemother, 2015. **59**(7): p. 4094-105.
41. Klock, H.E. and S.A. Lesley, *The Polymerase Incomplete Primer Extension (PIPE) method applied to high-throughput cloning and site-directed mutagenesis.* Methods Mol Biol, 2009. **498**: p. 91-103.
42. Kabsch, W., *XDS.* (1399-0047 (Electronic)).
43. Winn, M.D., et al., *Overview of the CCP4 suite and current developments.* (1399-0047 (Electronic)).
44. Sheldrick, G.M., *Experimental phasing with SHELXC/D/E: combining chain tracing with density modification.* (1399-0047 (Electronic)).
45. McCoy, A.J., et al., *Phaser crystallographic software.* J Appl Crystallogr, 2007. **40**(Pt 4): p. 658-674.
46. Cowtan, K., *Recent developments in classical density modification.* (1399-0047 (Electronic)).
47. Cowtan, K., *The Buccaneer software for automated model building. 1. Tracing protein chains.* (0907-4449 (Print)).
48. Kovalevskiy, O., et al., *Overview of refinement procedures within REFMAC5: utilizing data from different sources.* (2059-7983 (Electronic)).
49. Emsley, P., et al., *Features and development of Coot.* (1399-0047 (Electronic)).
50. Adams, P.D., et al., *PHENIX: a comprehensive Python-based system for macromolecular structure solution.* (1399-0047 (Electronic)).
51. Berman, H.M., et al., *The Protein Data Bank.* (0305-1048 (Print)).
52. Carvalho, F., et al., *Extraction of cell wall-bound teichoic acids and surface proteins from Listeria monocytogenes.* Methods Mol Biol, 2013. **966**: p. 289-308.
53. Cabanes, D., M. Lecuit, and P. Cossart, *Animal models of Listeria infection.* Curr Protoc Microbiol, 2008. **Chapter 9**: p. Unit9B 1.